nature chemistry

Article

https://doi.org/10.1038/s41557-023-01235-9

Metal-dependent enzyme symmetry guides the biosynthetic flux of terpene precursors

Received: 5 August 2022

Accepted: 10 May 2023

Published online: 12 June 2023

Check for updates

Felix Ecker[1], Abith Vattekkatte[2], Wilhelm Boland[2] ✉ & Michael Groll[1] ✉

Terpenoids account for more than 60% of all natural products, and their carbon skeletons originate from common isoprenoid units of different lengths such as geranyl pyrophosphate and farnesyl pyrophosphate. Here we characterize a metal-dependent, bifunctional isoprenyl diphosphate synthase from the leaf beetle *Phaedon cochleariae* by structural and functional analyses. Inter- and intramolecular cooperative effects in the homodimer strongly depend on the provided metal ions and regulate the biosynthetic flux of terpene precursors to either biological defence or physiological development. Strikingly, a unique chain length determination domain adapts to form geranyl or farnesyl pyrophosphate by altering enzyme symmetry and ligand affinity between both subunits. In addition, we identify an allosteric geranyl-pyrophosphate-specific binding site that shares similarity with end-product inhibition in human farnesyl pyrophosphate synthase. Our combined findings elucidate a deeply intertwined reaction mechanism in the *P. cochleariae* isoprenyl diphosphate synthase that integrates substrate, product and metal-ion concentrations to harness its dynamic potential.

Terpenes and terpenoids form the largest group of natural products, with currently over 80,000 known members, of which many display intriguing pharmaceutical properties[1]. Despite being chemically diverse agents of intraspecies and interspecies communication, as well as cellular integrity and proliferation, they emerge from only two isomeric building blocks, dimethylallyl pyrophosphate (DMAPP, C_5) and isopentenyl pyrophosphate (IPP, C_5)[2]. Short chain isoprenyl diphosphate synthases (scIDSs) elongate DMAPP to geranyl pyrophosphate (GPP, C_{10}) and further to farnesyl pyrophosphate (FPP, C_{15}) by consuming IPP in each step[3]. The uniform mechanism of this enzyme class requires three divalent cations that coordinate substrates at an allylic binding pocket (AI site) between the first and second aspartate-rich motif (FARM and SARM). The metal cluster provides an ionizing force that facilitates the dissociation of the pyrophosphate moiety (PP_{AI}) once IPP binds to basic residues at the proximal homoallylic site (HAI; Fig. 1). The terminal double bond of IPP_{HAI} attacks the nascent carbocation and connects the C_5 precursor with the prenyl unit. Ultimately, the released inorganic pyrophosphate (PP_i) deprotonates the extended metabolite at C_2 and forms the *trans* double bond. If the chain length determination domain of the enzyme provides access to the generated allylic product, the elongation reaction repeats[4].

FPP synthases (FPPSs) are distributed in all three kingdoms of life and catalyse both GPP and FPP formation, with the latter being the preferred reaction under physiological conditions. By contrast, GPP-specific synthases (GPPSs) are predominantly found in plants, but some insects, especially aphids and beetles, use GPP to yield defensive and pheromonal monoterpenes[5–7]. To date, only a single animal GPPS has been identified, in a bark beetle[8], suggesting that alternative regulatory mechanisms to accumulate GPP exist within the repertoire of FPPS. Indeed, several scIDSs in insects control the biosynthesis of mono- (C_{10}) and sesquiterpenes (C_{15}) to meet the organism's current needs[9–12]. Isoprenyl diphosphate synthase in *P. cochleariae* (PcIDS1, EC 2.5.1.1) produces FPP in the presence of Mg^{2+}, but preferably forms GPP when exposed to the heavy metal ions (HMIs) Co^{2+} or Mn^{2+}. Using C_{10} units as a building block, this leaf beetle secretes monoterpenes like chrysomeldial to protect itself against predation in its larval stadium. However, insects constantly require sesquiterpenoid hormones that drive large transformations during metamorphosis (Fig. 1b). Thus, balancing the

[1]Center for Protein Assemblies, Technical University of Munich, Garching, Germany. [2]Department of Bioorganic Chemistry, Max Planck Institute for Chemical Ecology, Jena, Germany. ✉e-mail: boland@ice.mpg.de; michael.groll@tum.de

https://doi.org/10.1038/s41557-023-01235-9

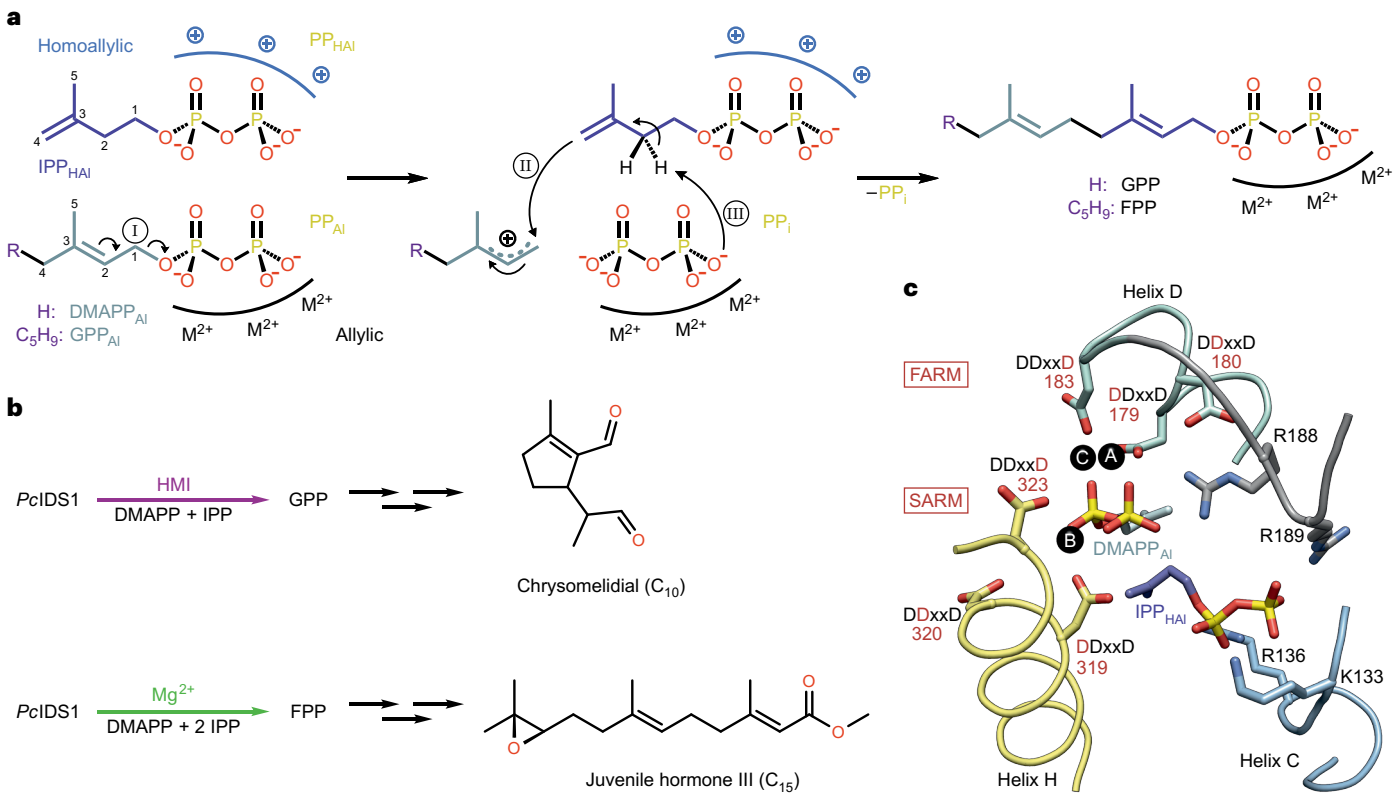

Fig. 1 | Reaction mechanism and substrate coordination in scIDS. a, Catalysis is uniform in this class of enzymes and starts with a prenyl substrate (DMAPP or GPP) bound to the allylic site (AI). A trinuclear, divalent metal cluster surrounds the pyrophosphate moiety (PP_{AI}) and facilitates ionization of the ester bond (I). Basic residues of the homoallylic site (HAI) bind IPP, which attacks the nascent carbocation at C_1 of the prenyl moiety (II). The generated inorganic pyrophosphate (PP_i) deprotonates at C_2 (III) of the intermediate and restores the allylic character of the elongated metabolite (GPP or FPP). **b**, In *P. cochleariae*, GPP is the main product of PcIDS1 in the presence of HMIs and precursor of the defensive monoterpene (C_{10}) chrysomelidial. FPP formation is driven by Mg^{2+} and essential for sesquiterpene hormones (C_{15}) during larval development. **c**, Active site architecture of scIDS enzymes shown for PcIDS1 in complex with $DMAPP_{AI}$ and IPP_{HAI}. The first and second aspartate-rich DDxxD motifs (FARM and SARM; D, aspartate; x, any amino acid; red numbers indicate residue position) on helix D and helix H coordinate Mg^{2+} at positions A, B and C. Colour coding is described in the Methods.

concentrations of terpene precursors in accordance with environmental and developmental demands is an essential cellular process[13].

Here we elucidate catalytic principles in PcIDS1 that either break or enforce dimer symmetry in response to HMIs. High-resolution crystal structures combined with functional and mutagenetic analyses reveal how different conformational states determine the product spectrum. In addition, a Mg^{2+}–water cluster was identified that regulates the elongation reaction by reducing the affinity for IPP. We demonstrate that Mg^{2+} deactivates one of both active sites in PcIDS1 during FPP formation, whereas HMIs recruit GPP to a specific, allosteric pocket similar to end-product inhibition in the human FPP synthase[14]. Overall, our combined findings provide insights into the biosynthetic flux of terpene precursors towards biological defence or physiological development.

Results

Compared to well-studied scIDS enzymes that specifically produce C_{10}, C_{15} or C_{20} isoprene precursors, the product chain length of PcIDS1 depends heavily on the provided metal cofactor. This synthase yields 96% GPP and only 4% FPP in the presence of Mn^{2+} or Co^{2+}, whereas 18% GPP and 82% FPP form with Mg^{2+} (ref. 10). To elucidate the HMI-dependent molecular processes that suppress FPP accumulation, PcIDS1 was recombinantly expressed and purified (Supplementary Fig. 1). Protein stability was optimal in $MgCl_2$ buffers and tolerated the addition of $MnCl_2$, while $CoCl_2$ facilitated precipitation. Next, we characterized the denaturation temperatures of different PcIDS1:metal:ligand complexes by thermal shift assays (Fig. 2a and Supplementary Fig. 2). In the absence of ligands, the stability of wild-type protein (41 °C) was not affected by Mn^{2+}. For the allylic substrate DMAPP, the temperature shift in the presence of Mn^{2+} (Δ10 °C) was much stronger compared to Mg^{2+} (Δ3 °C). This discrepancy correlates with the higher affinity of PcIDS1 for DMAPP with Mn^{2+} (ref. 10), which might allow DMAPP to occupy the HAI site at high concentrations[15]. A similar metal dependency was observed with IPP (Δ14 °C for Mn^{2+}, Δ7 °C for Mg^{2+}), further highlighting the preference of HMIs to coordinate C_5 substrates. The significant change in thermal stability with either metal suggests that IPP coordinates the HAI as well as the AI site in the absence of competing ligands. However, Mn^{2+} had no effect on the drastically increased protein stability (Δ28 °C) with the AI-specific ligand zoledronic acid (ZOL; ref. 16). The denaturation temperature, however, rose further when IPP was added (Δ37 °C), supposing that the inhibitor and substrate cooperatively interact with the AI site as well as the HAI site. For GPP, the product of the first elongation, the distinct thermal shift (Δ17 °C) was indifferent to the metal species, and FPP only had a moderate influence on protein stability (Δ5 °C for Mn^{2+}, Δ7 °C for Mg^{2+}). Therefore, our thermal shift assay results provide valuable information on ligand affinity to elucidate metal-dependent processes in PcIDS1 at the molecular level.

Catalytic principles of PcIDS1

To obtain molecular insights into PcIDS1, we first determined the apo crystal structure in the presence of Mg^{2+} (Protein Data Bank (PDB) 8A6U). The enzyme adopts the conserved scIDS topology (best distance matrix alignment (DALI) hit[17], PDB 3EWG, FPPS from *Trypanosoma*

https://doi.org/10.1038/s41557-023-01235-9

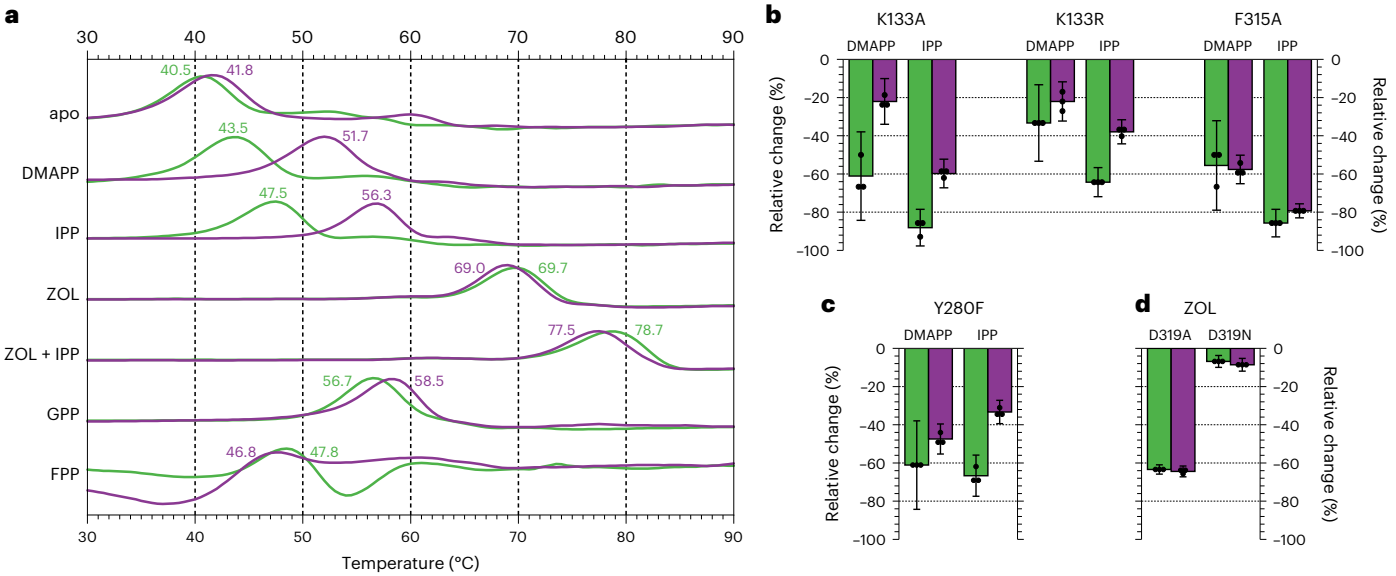

Fig. 2 | Thermal stability of PcIDS1:metal:ligand complexes. a, The fluorescence signal of recombinant PcIDS1 (6.25 µM) was recorded between 30 and 90 °C in the absence of (apo) and together with 200 µM of respective ligands. The graph displays the time-based derivative in relative units. The mean melting temperature is annotated in degrees Celsius next to the curves observed in $MgCl_2$ buffer alone (5 mM, green) and with $MnCl_2$ (1 mM, purple). **b**,**c**, Relative changes in thermal stability (compared to wild-type protein) for different protein mutants in the presence of DMAPP and IPP. **d**, ZOL binding stability in variants of the metal-coordinating SARM residue D319. Bars indicate the average value of three measurements (shown as dots); whiskers represent the relative error of the mean between mutant and wild-type protein. A detailed data analysis is in Supplementary Fig. 2.

brucei[18], Z-score (similarity of equivalent Cα-Cα distances among two proteins) 36.1, 30% sequence identity) with a dimer interface of 2,000 Å^2 (ref. 19). Each subunit (sub_A and sub_B) consists of 13 helices (αA to αJ and α1 to α3; Extended Data Fig. 1a). In both chains, the N terminus and C terminus as well as the loops between αD–αE (183–201) and αH–α1 (329–332) are disordered. The FARM region (179–183) is partially resolved, while D319 of the SARM (319–323) coordinates a pentahydrated Mg^{2+} at site B (Mg^{2+}_B).

Next, we determined a Mg^{2+}-bound IPP complex (PDB 8A6V) that shows significant discrepancies between the two subunits. Sub_A displays an open state and contains a single IPP molecule at the Al site with a 5 Å distance to Mg^{2+}_B, mimicking the native substrate DMAPP (Fig. 3a). D179 and D183 of the FARM rearrange and coordinate PP_{Al} in a staggered conformation by Mg^{2+}_A and Mg^{2+}_C. Surprisingly, the electron density map depicts an additional pentahydrated metal site (Mg^{2+}_D) at the β-phosphate ($P_β$) with a major impact on catalysis (as decribed in the following section). Binding of IPP_{Al} introduces a strong hydrogen bond between R188 and $P_β$ that reorders the residues of αD–αE into a defined substrate loop. Notably, R184 and F202 in this region engage in cation–π interactions with their equivalents in sub_B, indicating inter-subunit cooperativity between the Al sites (Fig. 4a).

However, sub_B forms the closed state with two IPP molecules and depicts extensive conformational changes compared to the open state (Fig. 3b and Supplementary Table 4). Here, the domain around the SARM is rearranged and pushed towards the Al site together with α3 and the N terminus of αI (Extended Data Fig. 2). The flexible region 327–336 forms a short α-helix that anchors K333 between PP_{Al} and D319 (Fig. 4b). This induced fit moves Mg^{2+}_B by 4 Å to interact with both phosphates of IPP_{Al}, while Mg^{2+}_D is released. Thereby, the PP_{Al} moiety is forced into an eclipsed configuration that promotes carbocation formation. Binding of the second IPP molecule to K133, R136 and R189 at the homoallylic site recruits the C terminus (425–429; Extended Data Fig. 1b). Stabilized by cation–π interactions with R427, the F315 side chain positions IPP_{HAl} for nucleophilic attack (Fig. 4c). These structural observations are supported by a decreased thermal resilience of the K133R, K133A and F315A variants in complex with DMAPP and IPP (Fig. 2b).

The comparison between the open (sub_A) and closed (sub_B) states reveals a feedback relation between the HAl and Al sites. Binding of IPP_{HAl} displaces interactions between E169, Q172 and Y280, resulting in a 120° clockwise rotation of the allylic prenyl unit (Fig. 4d and Supplementary Fig. 7c). The significantly reduced stability for DMAPP and IPP in the Y280F mutant indicates catalytic relevance of this regulatory cascade (Fig. 2c). Modelling of $DMAPP_{Al}$ and IPP_{HAl} into the active site shows that reorientation of the allylic substrate results in an ideal distance (3.2 Å) between its C_1 atom and the homoallylic double bond, facilitating C–C bond formation.

To investigate the second elongation step from GPP to FPP, we determined the complex structure of $PcIDS1_{Mg}$:GPP (PDB 8A70). In the presence of Mg^{2+}, GPP_{Al} binds to the metal cluster (A–D) at the Al site in sub_A (open state; Fig. 3d) and sub_B remains vacant. While GPP_{Al} adopts the binding mode of IPP_{Al} with C_1–C_5, the distal C_6–C_{10} unit inverts the M178 side chain and generates a spacious specificity pocket that is inaccessible in the IPP_{Al} complex. To elucidate the structural features of FPP formation in the closed state, we applied IPP together with a geranyl pyrophosphate derivative brominated at position C3 (3-Br-GPP). In this surrogate, the electrophilic bromine prevents carbocation formation and blocks catalysis[20]. Our crystallographic studies show that 3-Br-GPP mimics GPP_{Al} coordination, and the halogen atom occupies a similar position as the native 3-methyl group (Fig. 3e; PDB 8A7A). However, the HAl site remains vacant as 3-Br-GPP competes with IPP_{HAl} binding by stabilizing the open state through a polar interaction between Y280 and Br (Supplementary Fig. 4f). In the absence of experimental data, we modelled the active GPP_{Al}:IPP_{HAl} complex (Supplementary Fig. 7d). To reach the closed state, GPP_{Al} must undergo a similar reorientation as that of $DMAPP_{Al}$, suggesting that GPP and FPP syntheses follow the same catalytic process. Yet, the relationship between structure and product distribution remains unresolved.

Dimer symmetry governs product distribution

Structural analysis of $PcIDS1_{Mg}$:GPP (PDB 8A70) reveals an asymmetric complex in which the ligand is bound only to sub_A. This broken dimer symmetry originates from the C_{10} prenyl moiety that flips the side chain

https://doi.org/10.1038/s41557-023-01235-9

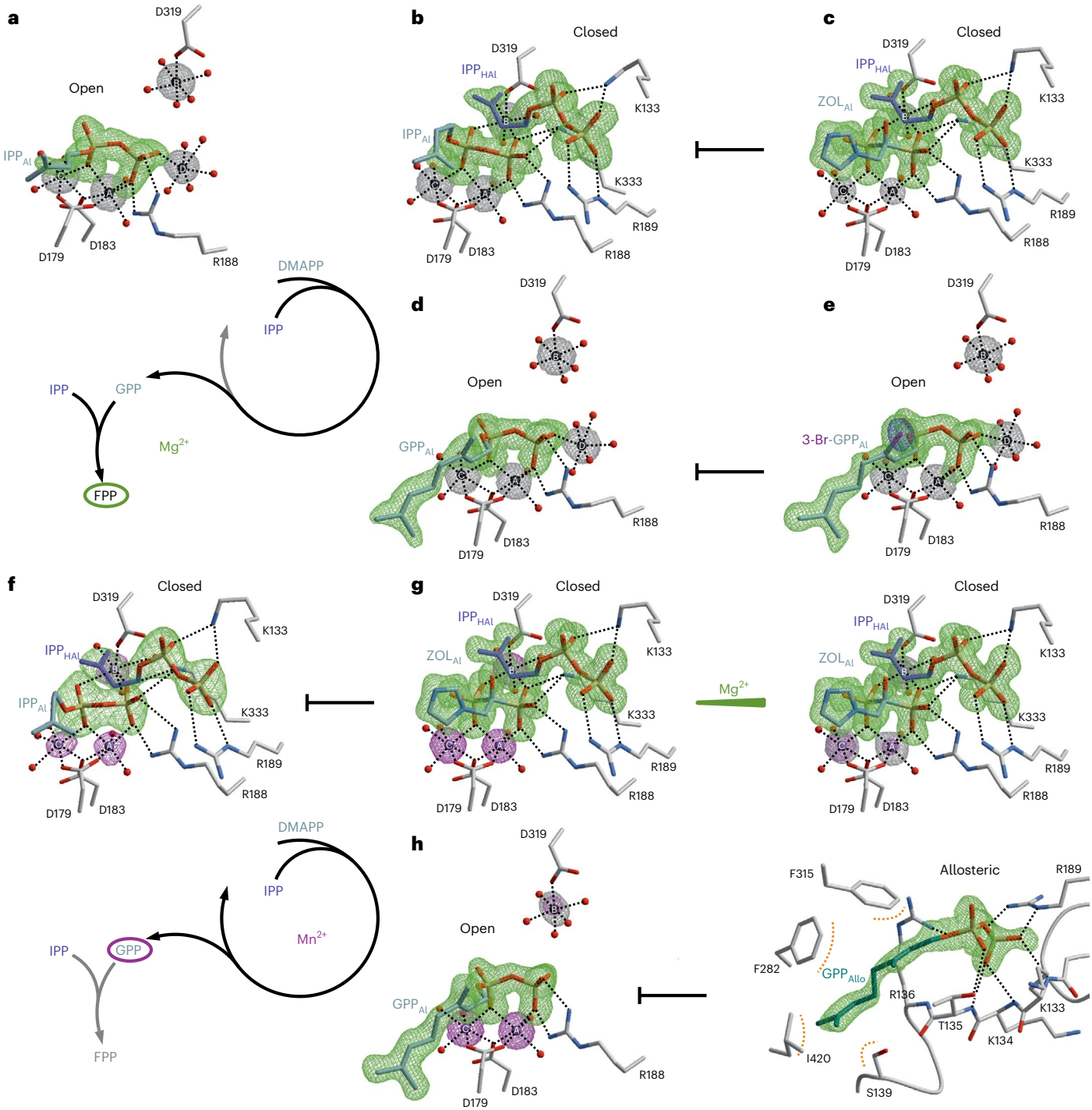

Fig. 3 | Mg^{2+} ions drive FPP production in PcIDS1. Snapshots of the active site during catalysis and in complex with inhibitors. Metal ions are drawn in black (Mg^{2+}) and pink (Mn^{2+}), H-bonds are illustrated as black dots. Omit electron density maps are shown in green (F_O–F_C, 3.0 σ), grey ($2F_O$–F_C, 1.0 σ), pink (ano Mn, 10.0 σ) and blue (ano Br, 10.0 σ). **a**, PcIDS1$_{Mg}$:IPP (PDB 8A6V); IPP imitates the native DMAPP$_{Al}$ moiety with a fourth Mg^{2+} (site D) coordinating $P_β$. **b**, PcIDS1$_{Mg}$:IPP:IPP (PDB 8A6V); a second IPP molecule binds to basic residues at the homoallylic site (HAl). Mg$^{2+}{}_B$ is pushed towards PP$_{Al}$, which adapts an eclipsed conformation to depart as PP$_i$. **c**, PcIDS1$_{Mg}$:ZOL:IPP (PDB 8A7C); the bisphosphonate inhibitor ZOL imitates PP$_{Al}$ coordination in the closed state. **d**, PcIDS1$_{Mg}$:GPP (PDB 8A70); upon prenyl elongation and PP$_i$ release, GPP binds to the allylic site (Al) in the open state. Site D is occupied by a pentahydrated Mg^{2+} ion. Mg^{2+} drives the repetition of the cycle to form FPP (left). **e**, PcIDS1$_{Mg}$:3-Br-GPP (PDB 8A7A); the bromine atom in 3-Br-GPP prevents carbocation formation. **f**, PcIDS1$_{Mn}$:IPP:IPP (PDB 8A6Z); both subunits form the closed state with IPP$_{Al}$ and IPP$_{HAl}$ with Mn^{2+} at a 100-fold excess of Mg^{2+}. **g**, PcIDS1$_{Mn}$:ZOL:IPP; the active site is occupied by Mn^{2+} at sites A through C in complex with the inhibitor ZOL$_{Al}$ and IPP$_{HAl}$ (right, PDB 8A7J). A 50-fold excess of Mg^{2+} reduces the anomalous signal at A and B (left, PDB 8A7K). **h**, PcIDS1$_{Mn}$:GPP:GPP (PDB 8A73); Mn$^{2+}{}_A$ and Mn$^{2+}{}_C$ sequester the PP$_{Al}$ moiety and prevent coordination of Mg$^{2+}{}_D$. A second GPP acts as an allosteric inhibitor (right). GPP is the main product of catalysis in the presence of Mn^{2+} (left). Inhibition arrows are highlighted in black. Colour coding is described in the Methods. A stereo version of this figure is presented in Extended Data Fig. 3. A comprehensive overview of all structures is shown in Supplementary Figs. 3–6.

https://doi.org/10.1038/s41557-023-01235-9

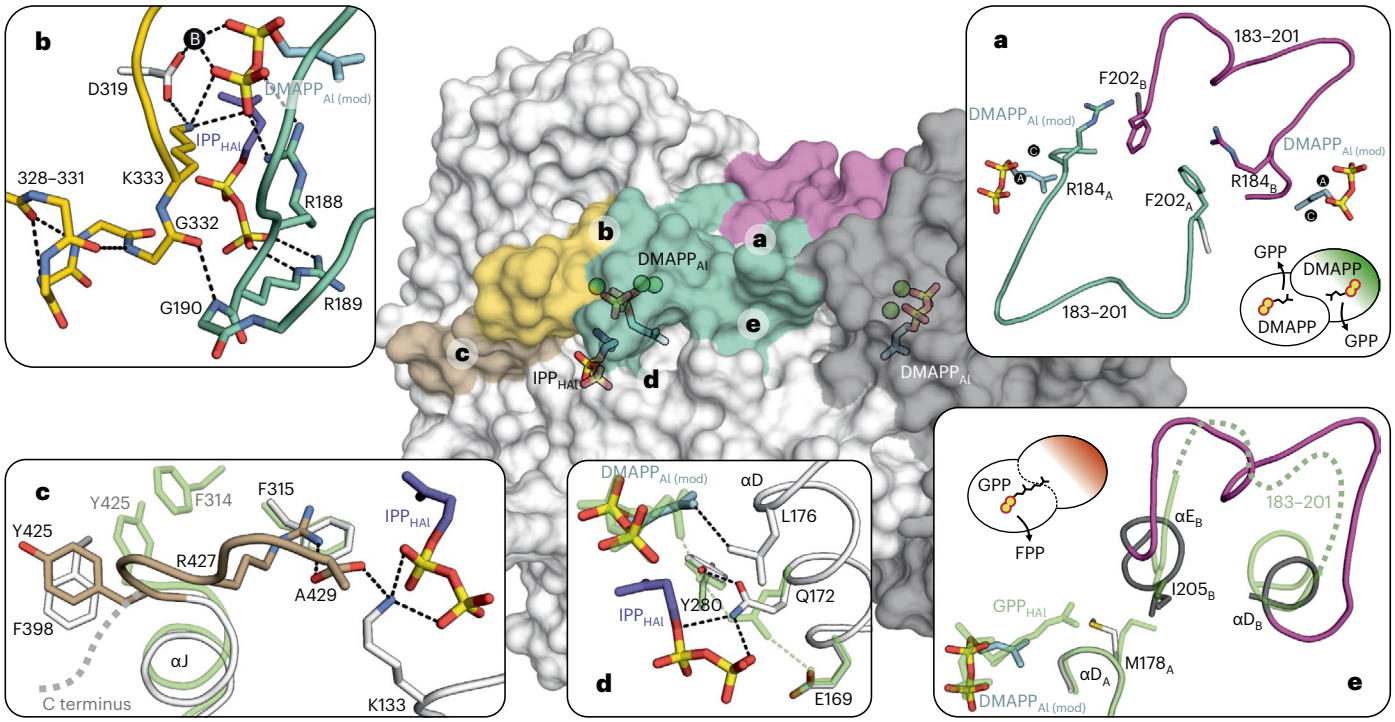

Fig. 4 | The regulatory framework of PcIDS1. Domains undergoing distinct conformational changes during catalysis are highlighted on a surface representation of $PcIDS1_{Mg}$:IPP:IPP (PDB 8A6V). DMAPP was modelled into the allylic site ($DMAPP_{Al\,(mod)}$) to chains A (white) and B (grey; Supplementary Fig. 7b). **a**, $DMAPP_{Al}$ induces substrate loop formation (183–201, mint) and initiates a cooperative effect on the second subunit through cation–π interactions between R184 and F202 residues (purple). GPP formation can occur in both active sites simultaneously (inset green scheme). **b**, IPP_{HAl} forms the closed state with R188 and R189 (mint) facing the PP moieties. D319 and metal B move towards $DMAPP_{Al}$ and stabilize the eclipsed PP conformation with K333 (gold). Thereby, residues 328–331 arrange into a helix and anchor the substrate loop. **c**, The C terminus (brown) is recruited from a dynamic state (green) by inverting Y425 to engage in π-stacking with F398. F315 selects for IPP_{HAl} and provides cation–π interactions to R427. The terminal carboxy group of A429 is located between R427 and K133, which stabilizes PP_{HAl}. **d**, In the presence of IPP_{HAl}, Q172 breaks the hydrogen bond to E169 (green) and displaces Y280, causing a rotation of the $DMAPP_{Al}$ prenyl moiety towards L176. **e**, The C_{10} prenyl chain of GPP disrupts the substrate loop at the N terminus of αE_B in the neighbouring subunit by pushing $M178_A$ into $I205_B$. PcIDS1 is a single-subunit catalyst for FPP production (inset red scheme). Colour coding is described in the Methods.

of M178 in sub_A and displaces I205 in the adjacent sub_B (Fig. 4e). The rearrangements disrupt the substrate loop and destabilize the Al and HAl sites of sub_B (Extended Data Fig. 4a). Interestingly, the structure of the F315A variant reveals that GPP_{Al} still binds to both subunits in response to a modified catalytic network (PDB 8A74; Extended Data Fig. 4b). While GPP_{Al} follows the described binding mode in sub_A, the orientation of M178 in sub_B forces the prenyl moiety of the ligand into a kinked conformation. This unphysiological state is stabilized by the metal cluster, and the substrate loop in sub_B is only defined at the FARM region. Although this asymmetric complex displays an affinity for ligands at the Al site, IPP_{HAl} cannot coordinate to sub_B unless GPP_{Al} dissociates from sub_A. In consequence, PcIDS1 acts as a single-subunit catalyst during FPP formation.

On the other hand, the $PcIDS1_{Mg}$ complex with IPP_{Al} (PDB 8A6V) displays intersubunit cooperativity between the two substrate loops. However, IPP_{HAl} is bound only to one subunit and does not prove that catalysis can take place simultaneously in both active sites. To obtain a symmetric complex with IPP_{HAl} in both subunits, a strong ligand for the Al site like ZOL is required. This inhibitor significantly increases the thermal stability of all PcIDS1 variants apart from D319A, which prevents coordination of $Mg^{2+}{}_B$ (Fig. 2 and Supplementary Figs. 2 and 4h). These results indicate that the PcIDS1:ZOL complex favours the closed state and induces formation of the HAl site, which is confirmed by the 9 °C shift upon addition of IPP. Indeed, the structure of $PcIDS1_{Mg}$:ZOL:IPP (PDB 8A7C) displays symmetry between sub_A and sub_B and mimics the active site prior to GPP synthesis (Fig. 3c). The protonated imidazole group of ZOL_{Al} imitates the nascent carbocation of $DMAPP_{Al}$, while the central hydroxymethyl group constrains the bisphosphonate to a fixed conformation. With four negative charges, bisphosphonate resembles the eclipsed PP_{Al} moiety and engages with all metal sites to induce IPP_{HAl} binding in its native orientation (Supplementary Fig. 5b). Thus, the binding strength of C_5 ligands at the Al site correlates with the affinity for IPP_{HAl} and promotes catalysis in both subunits.

Mn^{2+} ions increase affinity for the allylic ligand

To determine the binding mode of HMIs, we solved the crystal structure of $PcIDS1_{Mn}$:ZOL:IPP in a buffer containing a mixture of $MgCl_2$ and $MnCl_2$ (5:1 stoichiometry; PDB 8A7J). The subunits are identical to $PcIDS1_{Mg}$:ZOL:IPP (PDB 8A7C) apart from the anomalous Mn signal for all three metal positions (Fig. 3g, left and Supplementary Table 4). The influence of environmental HMI concentrations was evaluated by a second structure in the presence of 50-fold Mg^{2+} excess over Mn^{2+} (PDB 8A7K). Despite the abundance of Mg^{2+}, sites A and B still harbour Mn^{2+} (Fig. 3g, right), confirming the preference of the enzyme for ligands coordinated by HMIs. Unlike $Mn^{2+}{}_A$ and $Mn^{2+}{}_B$, which rest in a rigid, bidentate coordination with the phosphonate groups of ZOL_{Al}, position C can be selected through interactions with the FARM during substrate binding. Accordingly, $Mn^{2+}{}_C$ remains the dominant metal species even at high Mg^{2+} concentrations to enhance the ionization of P_α during catalysis and stabilize the nascent carbocation.

However, the enforced closed state through ZOL_{Al} coordination does not provide information about the metal-dependent interplay between the Al and HAl sites. Therefore, we applied IPP as a surrogate for $DMAPP_{Al}$ to evaluate Mn^{2+} binding in a native context and solved the structure of $PcIDS1_{Mn}$:IPP:IPP (PDB 8A6Z). The complex forms a

https://doi.org/10.1038/s41557-023-01235-9

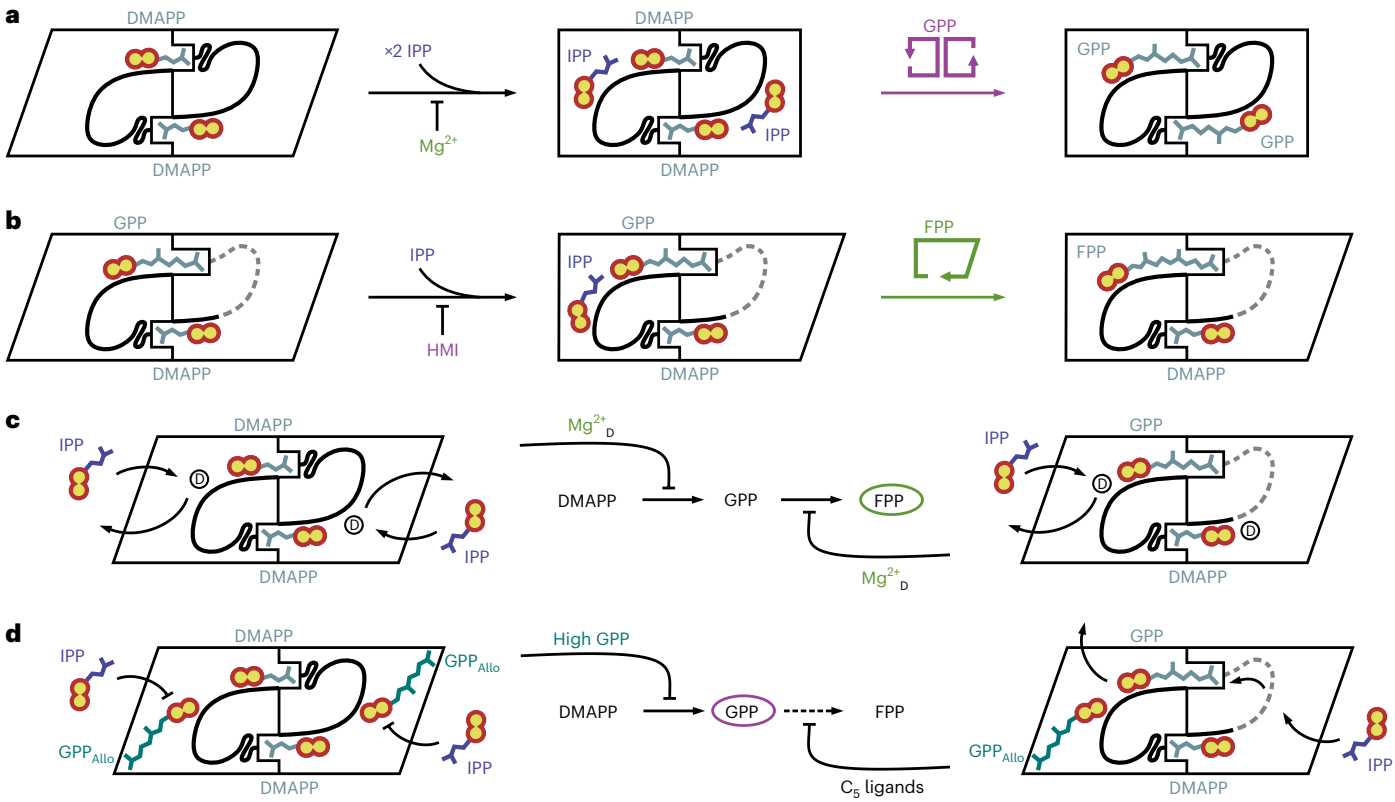

Fig. 5 | Regulation of PcIDS1 catalysis. The two subunits of the homodimer (sub_A and sub_B) are depicted in either the open (rhombic) or closed (rectangle) state. Substrate loops are drawn in black with unstructured regions as grey dashes. **a**, PcIDS1 catalyses the reaction of DMAPP and IPP to GPP in both subunits at the same time (symmetric, pink scheme). HMIs accelerate the transition to the closed state, while Mg^{2+} slows down catalysis. **b**, The enzyme procedurally converts GPP and IPP to FPP in a single subunit (asymmetric, green scheme). HMIs counteract GPP_{AI} coordination, while Mg^{2+} stabilizes the open state. **c**, $Mg^{2+}{}_D$ represents a modulator of IPP_{HAI} binding during GPP (left) and FPP (right) synthesis. **d**, In the presence of HMIs, GPP_{Allo} binds to both substrate loops and prevents GPP accumulation (left). GPP_{Allo} binds only to sub_A (right), and C_5 ligands that coordinate to sub_B displace GPP_{AI} from sub_A to counteract FPP formation (dashed arrow). An extended reaction network is provided in Supplementary Fig. 11.

symmetric dimer with IPP_{AI} and IPP_{HAI} in the closed state and is similar to sub_B of $PcIDS1_{Mg}$:IPP:IPP (PDB 8A6V; Supplementary Fig. 3f). Remarkably, the three metal positions depict a uniform anomalous density for Mn^{2+} despite a 100-fold Mg^{2+} excess in the crystallization buffer (Fig. 3f). Thus, in the absence of IPP_{HAI}, the staggered configuration of PP_{AI} selects for $Mn^{2+}{}_A$ and $Mn^{2+}{}_C$. Once IPP coordinates the HAI site, the high affinity of Mn^{2+} replaces $Mg^{2+}{}_B$ and stabilizes the eclipsed orientation of PP_{AI}, driving PP_i release.

So far, the described Mn^{2+}-bound complexes all form symmetric homodimers with ligands at both AI and HAI sites. To determine whether HMIs are also recruited to asymmetric arrangements like those in $PcIDS1_{Mg}$:IPP or $PcIDS1_{Mg}$:GPP, we solved the structure of $PcIDS1_{Mn}$:GPP (PDB 8A73). With both subunits in the open state, GPP_{AI} is bound only to sub_A. While $Mn^{2+}{}_A$ and $Mn^{2+}{}_C$ coordinate GPP_{AI}, the pentameric water cluster at site B favours Mg^{2+} (Fig. 3h). Interestingly, the complex lacks electron density for a metal at site D, as observed in $PcIDS1_{Mg}$:GPP (PDB 8A70). Apparently, the stronger Lewis acidity of $Mn^{2+}{}_A$ and $Mn^{2+}{}_C$ reduces the charge density of PP_{AI} and prevents coordination of $Mg^{2+}{}_D$. Without this auxiliary metal cluster, P_β moves 1.0 Å towards the SARM and interacts with the hydration sphere of $Mg^{2+}{}_B$ (Supplementary Fig. 8). These rearrangements align the subunit for IPP_{HAI} coordination and facilitate the transition to the closed state. In consequence, HMIs enhance the intramolecular effect that forms the HAI site when a ligand is bound to AI. This cooperativity stabilizes both HAI sites during GPP synthesis but is limited to sub_A upon elongation to FPP. Therefore, HMIs counteract FPP formation by recruiting IPP_{HAI} to sub_B and displacing GPP_{AI} from sub_A.

Mn^{2+} recruits GPP to an allosteric pocket

The structure of $PcIDS1_{Mn}$:GPP (PDB 8A73) contains well-defined electron density for a second GPP molecule (GPP_{Allo}; Fig. 3h) that is absent in the Mg^{2+}-bound complex. Its prenyl moiety protrudes into a 7-Å-wide and 15-Å-deep channel between αC and αG as well as αJ in sub_A. V286 and I420 form the bottom of this specificity pocket and act as a molecular ruler, whereas F282 and F315 engage in π-stacking with both allyl groups. Notably, the PP moiety of this allosteric ligand coordinates with residues of the HAI site. While R136 contacts both phosphates, P_β is further stabilized by the αC helix dipole and forms a salt bridge with R189 of the substrate loop. GPP_{Allo} keeps the subunit in the open conformation, but the C terminus is directed towards the HAI site, and residues 328–331 form the helical turn as seen in $PcIDS1_{Mn}$:IPP:IPP (PDB 8A6Z). These findings indicate that IPP_{HAI} binding and GPP_{Allo} binding are mutually exclusive, and both depend on the intramolecular effect of HMIs. To elucidate the architecture of the allosteric site in the closed state, we determined the structure of $PcIDS1_{Mg}$:ZOL:GPP (PDB 8A7L). In this complex, ZOL_{AI} displaces GPP_{AI}, and the structural rearrangements prevent formation of the allosteric specificity pocket (Supplementary Fig. 6c). However, GPP still binds to the HAI site by inverting its PP moiety and exposing the prenyl unit towards the protein surface. Taken together, GPP_{Allo} represents a competitive inhibitor to IPP_{HAI} that stabilizes the open state in the presence of HMIs.

Discussion

Our study reveals how PcIDS1 couples metal coordination and dimer symmetry with an allosteric site to fine-tune product distribution

during the life cycle of *P. cochleariae*. In this enzyme, diversified regulatory domains evolved from a common scIDS topology to steer the biosynthetic flux of defensive monoterpene or hormonal sesquiterpene precursors. Exogenous metal cofactors shift the product distribution from FPP to GPP. Compared with the abundance of Mg^{2+} in the larval fat body tissue, Mn^{2+} and Co^{2+} are found at a ratio of 1:300 and 1:20,000, respectively[10]. HMIs compensate these low intracellular concentrations with their strong Lewis acidity and engage in stable substrate complexes that bind to PcIDS1 (refs. 21,22). Since HMIs accelerate GPP and FPP formation to the same extent, they exploit additional mechanisms to alter product distribution[10,22–25].

Symmetry is a common regulatory principle in scIDS enzymes that use the dimer interface to form selective binding sites for their allylic substrates. While heterodimeric GPPSs with a single active site have been identified[26], PcIDS1 enters the reaction as a symmetric homodimer. For GPP synthesis, $DMAPP_{Al}$ promotes intersubunit cooperativity and induces structural rearrangements that enable IPP_{HAl} binding. Compared to the apo enzyme, the thermal resilience of PcIDS1:DMAPP is increased, but an even stronger effect is seen for IPP (Fig. 2a). Combined with crystallographic studies, these findings prove a competitive inhibition of IPP_{Al} at high concentrations by binding to the open state as well as the closed state[10,27,28]. In addition, with either IPP_{HAl} or $DMAPP_{HAl}$, HMIs abolish $Mg^{2+}{}_{D}$ coordination at PP_{Al} and enhance GPP formation (Fig. 5a). This metal-dependent cross-talk between the Al and HAl sites results in improved protein stability with both C_5 ligands and agrees with previous kinetic studies[10].

Once GPP is formed, it can either dissociate to enter monoterpene biosynthesis or proceed to the Al site for further elongation. Binding of GPP_{Al}, however, breaks the dimer symmetry and restricts catalysis to one active site for FPP synthesis (Fig. 5b). Key to this asymmetry is the unique chain length determination domain sequence SLxxM (located at −5 to −1 upstream of the FARM; S, serine; L, leucine; M, methionine; x, any amino acid). So far, characterized scIDSs harbour aromatic sidechains at −5 and −4 that mediate substrate selectivity, and a small residue at −1 (refs. 4,29–32). In PcIDS1, S174 of the chain length determination domain motif provides stability at the dimer interface, and L175 forms a hydrophobic patch that guides GPP_{Al} towards M178. An induced flip of the methionine side chain restricts GPP_{Al} to one active site at a time. Such a regulatory connection between distant active sites of homodimeric enzymes was recently described for the human transketolase and represents a fundamental principle of positive or negative cooperativity[33]. Notably, methionine at −1 is conserved in a mosquito scIDS with similar metal-dependent product regulation to PcIDS1 (ref. 11).

The binding mode of GPP_{Al} involves significant hydrophobic contacts that stabilize the complex and are independent from the metal cluster at Al. During FPP formation in the presence of Mg^{2+}, the additional metal site D, however, decelerates the reaction rate[10] and selectively recruits IPP_{HAl} only to the catalytic subunit (Fig. 5c). HMIs, on the other hand, put the asymmetric GPP_{Al} complex at a disadvantage by simultaneously increasing the affinity of C_5 ligands to all Al and HAl sites. In consequence, IPP_{HAl} binding to the disrupted subunit counteracts GPP_{Al} coordination (Fig. 5d). This results in a 20-fold decreased GPP affinity when IPP is applied with HMIs during FPP formation[10]. Thus, HMIs will always prefer the symmetric state with two stabilized substrate loops and accelerate GPP synthesis under physiological conditions.

To prevent GPP accumulation, HMIs fine-tune PcIDS1 activity by generating an allosteric binding site (Fig. 5d). The C_{10} prenyl unit of GPP_{Allo} protrudes into a hydrophobic channel, while the PP_{Allo} moiety competes with IPP_{HAl}. This coordination turns the product GPP into an allosteric inhibitor and slows down catalysis by trapping the subunit in a transition state (Supplementary Fig. 9). A similar regulation has been characterized for a C_{15}-specific binding site in human FPPS (HsFPPS) that mediates end-product inhibition[14]. However, the human FPP_{Allo} does not interact with the substrate loop and protrudes into a 4-Å-deeper cavity by inverting the prenyl moiety. This orientation is stabilized by L344, whereas the corresponding I420 in PcIDS1 tailors the allosteric binding channel to GPP (Supplementary Fig. 10). When this amino acid is replaced with alanine, the size of the cavity increases, but neither FPP_{Allo}, nor GPP_{Allo}, nor Mn^{2+} at the Al site are observed in the mutant structure (Supplementary Fig. 6d; PDB 8A7R). These findings highlight that the conserved architecture of allo sites has diverged into distinct roles during evolution. GPP_{Allo} in PcIDS1 is strictly dependent on the allylic metal cluster that induces formation of the HAl site and features a unique mode of action.

Our present study highlights an intricate reaction network for PcIDS1 that combines inter- and intramolecular effects with allosteric regulation. As indicated by previous kinetic assays, HMIs attain a high affinity for $DMAPP_{Al}$ (Michaelis constant (K_m) = 11.6 μM) and IPP_{HAl} (K_m = 0.84 μM) through cooperative symmetry between the subunits[10]. However, if DMAPP and IPP deplete during GPP accumulation, GPP_{Allo} could promote allosteric feedback and throttle the impact of HMIs on the reaction rate. PcIDS1 catalyses the first elongation step significantly slower with Mg^{2+} alone (25% of maximum velocity of the enzymatic reaction (v_{max})) and instead displays higher affinity for GPP_{Al} (K_m = 1.2 μM)[10]. Our crystal structures highlight that Mg^{2+} stabilizes an asymmetric complex with half-site reactivity to produce FPP, the precursor of sesquiterpene hormones. In vivo, an influx of exogenous HMI cofactors counteracts this second reaction and guides synthesis back to GPP (Supplementary Fig. 11). Thus, the dynamic nature of PcIDS1 allows *P. cochleariae* to fine-tune its terpene metabolism in response to environmental trigger factors during all life stages.

Online content

Any methods, additional references, Nature Portfolio reporting summaries, source data, extended data, supplementary information, acknowledgements, peer review information; details of author contributions and competing interests; and statements of data and code availability are available at https://doi.org/10.1038/s41557-023-01235-9.

References

1. Buckingham, J. *Natural Products Desk Reference* (CRC Press, 2017).
2. Hillier, S. G. & Lathe, R. Terpenes, hormones and life: isoprene rule revisited. *J. Endocrinol.* **242**, R9–R22 (2019).
3. Wang, K. Isoprenyl diphosphate synthases. *Biochim. Biophys. Acta Mol. Cell Biol. Lipids* **1529**, 33–48 (2000).
4. Tarshis, L. C., Proteau, P. J., Kellogg, B. A., Sacchettini, J. C. & Poulter, C. D. Regulation of product chain length by isoprenyl diphosphate synthases. *Proc. Natl Acad. Sci. USA* **93**, 15018–15023 (1996).
5. Cusson, M. et al. Biosynthesis and release of juvenile hormone and its precursors in insects and crustaceans: the search for a unifying arthropod endocrinology. *Insect Biochem.* **21**, 1–6 (1991).
6. Kislow, C. J. & Edwards, L. J. Repellent odour in aphids. *Nature.* **235**, 108–109 (1972).
7. Weibel, D. B. et al. Iridoid biosynthesis in staphylinid rove beetles (Coleoptera: Staphylinidae, Philonthinae). *Insect Biochem. Mol. Biol.* **31**, 583–591 (2001).
8. Gilg, A. B., Bearfield, J. C., Tittiger, C., Welch, W. H. & Blomquist, G. J. Isolation and functional expression of an animal geranyl diphosphate synthase and its role in bark beetle pheromone biosynthesis. *Proc. Natl Acad. Sci. USA* **102**, 9760–9765 (2005).
9. Vandermoten, S. et al. Characterization of a novel aphid prenyltransferase displaying dual geranyl/farnesyl diphosphate synthase activity. *FEBS Lett.* **582**, 1928–1934 (2008).
10. Frick, S. et al. Metal ions control product specificity of isoprenyl diphosphate synthases in the insect terpenoid pathway. *Proc. Natl Acad. Sci. USA* **110**, 4194–4199 (2013).

11. Rivera-Perez, C., Nyati, P. & Noriega, F. G. A corpora allata farnesyl diphosphate synthase in mosquitoes displaying a metal ion dependent substrate specificity. *Insect Biochem. Mol. Biol.* **64**, 44–50 (2015).
12. Vandermoten, S. et al. Structural features conferring dual geranyl/farnesyl diphosphate synthase activity to an aphid prenyltransferase. *Insect Biochem. Mol. Biol.* **39**, 707–716 (2009).
13. Nagel, R., Schmidt, A. & Peters, R. J. Isoprenyl diphosphate synthases: the chain length determining step in terpene biosynthesis. *Planta* **249**, 9–20 (2019).
14. Park, J., Zielinski, M., Magder, A., Tsantrizos, Y. S. & Berghuis, A. M. Human farnesyl pyrophosphate synthase is allosterically inhibited by its own product. *Nat. Commun.* **8**, 14132 (2017).
15. Gabelli, S. B. et al. Structure and mechanism of the farnesyl diphosphate synthase from *Trypanosoma cruzi*: implications for drug design. *Proteins* **62**, 80–88 (2006).
16. Ling, Y., Li, Z.-H., Miranda, K., Oldfield, E. & Moreno, S. N. J. The farnesyl-diphosphate/geranylgeranyl-diphosphate synthase of *Toxoplasma gondii* is a bifunctional enzyme and a molecular target of bisphosphonates. *J. Biol. Chem.* **282**, 30804–30816 (2007).
17. Holm, L. Using Dali for protein structure comparison. *Methods Mol. Biol.* **2112**, 29–42 (2020).
18. Mao, J. et al. Solid-state NMR, crystallographic, and computational investigation of bisphosphonates and farnesyl diphosphate synthase-bisphosphonate complexes. *J. Am. Chem. Soc.* **128**, 14485–14497 (2006).
19. Krissinel, E. & Henrick, K. Inference of macromolecular assemblies from crystalline state. *J. Mol. Biol.* **372**, 774–797 (2007).
20. Vattekkatte, A., Gatto, N., Schulze, E., Brandt, W. & Boland, W. Inhibition of a multiproduct terpene synthase from *Medicago truncatula* by 3-bromoprenyl diphosphates. *Org. Biomol. Chem.* **13**, 4776–4784 (2015).
21. Trachtman, M., Markham, G. D., Glusker, J. P., George, P. & Bock, C. W. Interactions of metal ions with water: ab initio molecular orbital studies of structure, bonding enthalpies, vibrational frequencies and charge distributions. 1. Monohydrates. *Inorg. Chem.* **37**, 4421–4431 (1998).
22. Bock, C. W., Katz, A. K., Markham, G. D. & Glusker, J. P. Manganese as a replacement for magnesium and zinc: functional comparison of the divalent ions. *J. Am. Chem. Soc.* **121**, 7360–7372 (1999).
23. Sissi, C. & Palumbo, M. Effects of magnesium and related divalent metal ions in topoisomerase structure and function. *Nucleic Acids Res.* **37**, 702–711 (2009).
24. Dismukes, G. C. Manganese enzymes with binuclear active sites. *Chem. Rev.* **96**, 2909–2926 (1996).
25. Irving, H. & Williams, R. J. P. Order of stability of metal complexes. *Nature* **162**, 746–747 (1948).
26. Chang, T.-H. et al. Structure of a heterotetrameric geranyl pyrophosphate synthase from mint (*Mentha piperita*) reveals intersubunit regulation. *Plant Cell* **22**, 454–467 (2010).
27. Reed, B. C. & Rilling, H. C. Substrate binding of avian liver prenyltransferase. *Biochemistry.* **15**, 3739–3745 (1976).
28. Barnard, G. F. & Popják, G. Human liver prenyltransferase and its characterization. *Biochim. Biophys. Acta Enzymol.* **661**, 87–99 (1981).
29. Wang, K. & Ohnuma, S. Chain-length determination mechanism of isoprenyl diphosphate synthases and implications for molecular evolution. *Trends Biochem. Sci.* **24**, 445–451 (1999).
30. Vandermoten, S., Haubruge, E. & Cusson, M. New insights into short-chain prenyltransferases: structural features, evolutionary history and potential for selective inhibition. *Cell. Mol. Life Sci.* **66**, 3685–3695 (2009).
31. Stanley Fernandez, S. M., Kellogg, B. A. & Poulter, C. D. Farnesyl diphosphate synthase. Altering the catalytic site to select for geranyl diphosphate activity. *Biochemistry* **39**, 15316–15321 (2000).
32. Narita, K., Ohnuma, S. & Nishino, T. Protein design of geranyl diphosphate synthase. Structural features that define the product specificities of prenyltransferases. *J. Biochem.* **126**, 566–571 (1999).
33. Dai, S. et al. Low-barrier hydrogen bonds in enzyme cooperativity. *Nature* **573**, 609–613 (2019).

Methods

Bacterial culture

The gene of PcIDS1 (GenBank AGE89831.1), which lacks the N-terminal signal peptide (residues 1 to 85)[10], was cloned into a pET-28b expression vector modified to encode an N-terminal His_6-SUMO tag. Site-directed mutagenesis (Supplementary Table 1) was performed with the QuikChange II kit (Agilent Technologies) according to the manufacturer's instructions and verified by Sanger sequencing (GATC Biotech). *Escherichia coli* K12 BL21(DE3) cells were transformed by electroporation and grown in glass shake flasks containing 2 l lysogenic broth (50 mg l^{-1} kanamycin) at 37 °C. After reaching an optical density measured at a wavelength of 600 nm (OD_{600}) of 0.6, flasks were stored at 4 °C for 30 minutes before adding 1 mM isopropylthiogalactoside (final concentration) to induce protein expression, which occurred overnight at 20 °C. Cell pellets were collected by centrifugation, washed once with 0.9% (w/v) NaCl and stored at −20 °C.

Protein purification

E. coli pellets of 10 g were dissolved in 50 ml buffer A (100 mM Tris/HCl pH 7.5, 500 mM NaCl, 10% (v/v) glycerol, 20 mM imidazole, 10 mM 2-mercaptoethanol (β-ME), 5 mM $MgCl_2$) and solubilized by sonication (Branson Digital Sonifier 250). After centrifugation (40,000*g*, 4 °C, 30 min), the supernatant was applied (5 ml min^{-1}) to a 5 ml HisTrap HP column with an ÄKTA Pure system (GE Healthcare), previously equilibrated with buffer A. Buffer A containing 5% buffer B (buffer A with 500 mM imidazole) was used to wash the column until the absorbance signal (280 nm) returned to the baseline. The protein of interest was eluted by a linear gradient (5–100% buffer B) within 50 ml total volume. Fractions containing sufficient concentrations of pure protein were pooled and spiked with 0.5 mg SUMO protease (Ulp1 from *Saccharomyces cerevisiae*) and dialysed overnight at 4 °C against 5 l buffer C (20 mM Tris/HCl pH 7.5, 100 mM NaCl, 10% (v/v) glycerol, 1 mM β-ME, 5 mM $MgCl_2$). HisTrap affinity chromatography was repeated, and the flow-through was concentrated to 2 ml using Amicon Ultra-15 centrifugal filters. Centrifugation (20,000*g*, 4 °C, 10 min) removed residual protein aggregates, and the supernatant was used for size exclusion chromatography with a HiLoad Superdex 200 16/60 column in buffer D (buffer C containing 1 mM tris(2-carboxyethyl)phosphine (TCEP) instead of β-ME) at 1.5 ml min^{-1}. High purity peak fractions were pooled, concentrated to at least 40 mg ml^{-1} (1 mM) and either used immediately or stored at −80 °C.

Thermal shift assay

A 96-well transparent polymerase chain reaction plate was prepared with 17 µl buffer in each well (final concentrations, 100 mM MES buffer pH 7.0, 100 mM NaCl, 10% (v/v) glycerol, 5 mM $MgCl_2$, 2.5 mM TCEP) both with and without addition of 1 mM $MnCl_2$. Ligand molecules (in 1 µl H_2O) were added to achieve final concentrations of 25 and 200 µM, respectively. In the presence of ZOL, IPP and GPP were applied at 100 µM. Some 1 µl of a 0.25 mg ml^{-1} protein–buffer solution (6.25 µM final concentration) was added using a Phoenix nano-dispenser system (Art Robbins Instruments), followed by 1 µl of an aqueous 1:40 dilution of Sypro Orange Stain (Merck). Plates were sealed, carefully shaken and centrifuged (1,000*g*, 4 °C, 5 min) to remove air bubbles. All samples were equilibrated to 4 °C in a CFX96 reverse transcriptase-polymerase chain reaction (RT-PCR) system (Biorad), and emission was detected while the temperature increased by 0.5 °C in 10 s intervals to 95 °C. Melting temperatures were derived from the inflection points of the fluorescence signal with CFX Maestro (v.4.1) and analysed (in triplicate) with OriginPro 2020 (v.9.7.0.185).

Protein crystallization and structure determination

Crystals of PcIDS1 wild-type and mutant proteins were grown using sitting drop vapour diffusion at 20 °C. Protein samples were applied at 20 mg ml^{-1} in buffer D (with/without 1 mM $MnCl_2$) and mixed with reservoir solution by an Oryx4 system (Douglas Instruments). Droplet compositions including the applied ligand molecules (2 mM, 1 mM for ZOL) are denoted in Supplementary Table 2. Diffracting crystals grew within a few weeks and were cryoprotected by adding 1 µl of mother liquor containing 30% (v/v) glycerol prior to vitrification in liquid nitrogen.

Native datasets were collected at beamline X06SA (Swiss Light Source, Paul Scherrer Institute, Villigen, Switzerland) with synchrotron radiation (wavelength $\lambda = 1.0$ Å). Anomalous scattering was additionally recorded at 1.89 Å (Mn) or 0.92 Å (Br) for crystals grown in the presence of $MnCl_2$ and 3-Br-GPP, respectively. Diffraction intensity data were evaluated by the XDS program and processed with XSCALE (Supplementary Table 3)[34]. Resolution limits were chosen to meet the following criteria: signal to noise ratio $I/\sigma(I) > 2.0$, statistic for the precision of the measurements of each unique reflection $R_{merge} < 70\%$ and redundancy of >3.0 (Supplementary Table 3). The initial structure of PcIDS1 was solved in space group $P2_1$ (PDB 8A6U). The structure of FPPS from *Gallus gallus* (PDB 1UBX; ref. 4) was used for molecular replacement by Patterson search calculations with Phaser[35]. All other PcIDS1 structures were determined using the apo structure. Models were built, refined and completed with cofactors and ligands in COOT[36] with intermittent, restrained refinements using REFMAC5 (ref. 37). Water molecules were positioned by ARP/wARP solvent[38]. TLS (Translation/Libration/Screw) and restrained refinements yielded adequate model parameters (Supplementary Table 3) as well as root-mean-square deviation (r.m.s.d.) values of bond lengths and angles (validated by PROCHECK[39]). To identify Mn and Br positions in the protein–ligand complex, anomalous difference Patterson maps were calculated with fast Fourier transformation[40]. The crystal structures were deposited in the RCSB Protein Data Bank (Supplementary Table 3).

Figure illustration

To systematically characterize substrate coordination in PcIDS1, figures were prepared with Molscript/Bobscript[41]. Protein residues (grey, marked by a one-letter code) and ligands at the allylic (Al, cyan), homoallylic (HAl, purple) and allosteric (Allo, teal) sites are shown as sticks. Mg^{2+} ions (black), Mn^{2+} ions (pink) and water molecules (red) are depicted as balls with cluster interactions represented by black dashes. Structural superpositions with PyMol (ref. 42) highlight discrepancies at the active site (coloured and grey). Unless noted otherwise, all electron density maps are F_O-F_C (green or blue mesh, contoured to 3.0 σ) or anomalous signal maps (pink for Mn and blue mesh for Br, 10.0 σ) with respective ligands omitted prior to phasing. The $2F_O-F_C$ maps around Mg^{2+} ions are contoured to 1.0 σ and coloured grey. Calculations combine the observed diffraction data, F_O, with the diffraction data calculated from the atomic model, F_C; σ represents the density value above the average value.

Annotations

The r.m.s.d. values were calculated for the Cα backbone with Top3D (ref. 43) and are annotated in Supplementary Table 4.

Reporting summary

Further information on research design is available in the Nature Portfolio Reporting Summary linked to this article.

Data availability

Crystallographic data were deposited in the RCSB Protein Data Bank with the PDB identification numbers 8A6U, 8A6V, 8A6Z, 8A70, 8A73, 8A74, 8A78, 8A7A, 8A7B, 8A7C, 8A7J, 8A7K, 8A7L, 8A7R and 8A7U. All other data are available in the text or in the Supplementary Information.

References

34. Kabsch, W. XDS. *Acta Crystallogr. D Biol. Crystallogr.* **66**, 125–132 (2010).

35. McCoy, A. J. et al. Phaser crystallographic software. *J. Appl. Crystallogr.* **40**, 658–674 (2007).
36. Emsley, P., Lohkamp, B., Scott, W. G. & Cowtan, K. Features and development of Coot. *Acta Crystallogr. D Biol. Crystallogr.* **66**, 486–501 (2010).
37. Murshudov, G. N. et al. REFMAC5 for the refinement of macromolecular crystal structures. *Acta Crystallogr. D Biol. Crystallogr.* **67**, 355–367 (2011).
38. Langer, G., Cohen, S. X., Lamzin, V. S. & Perrakis, A. Automated macromolecular model building for X-ray crystallography using ARP/wARP version 7. *Nat. Protoc.* **3**, 1171–1179 (2008).
39. Laskowski, R. A., MacArthur, M. W., Moss, D. S. & Thornton, J. M. PROCHECK. *J. Appl. Crystallogr.* **26**, 283–291 (1993).
40. Read, R. J. & Schierbeek, A. J. A phased translation function. *J. Appl. Crystallogr.* **21**, 490–495 (1988).
41. Kraulis, P. J. MOLSCRIPT: a program to produce both detailed and schematic plots of protein structures. *J. Appl. Crystallogr.* **24**, 946–950 (1991).
42. Delano, W. L. *The PyMOL Molecular Graphics System* (Schrödinger, 2002).
43. Winn, M. D. et al. Overview of the CCP4 suite and current developments. *Acta Crystallogr. D Biol. Crystallogr.* **67**, 235–242 (2011).

Acknowledgements

This research was supported by the German Research Foundation (DFG, grant no. 1861/5-2) and the Max Planck Society. We thank E. M. Huber for valuable input during manuscript preparation and the staff of beamline X06SA at the Paul Scherrer Institute, SLS, Villigen (Switzerland) for assistance during data collection.

Author contributions

F.E., A.V., W.B. and M.G. designed, conducted and analysed the experiments. F.E. and M.G. draughted the paper.

Funding

Open access funding provided by Max Planck Society.

Competing interests

The authors declare no competing interests.

Additional information

Extended data is available for this paper at https://doi.org/10.1038/s41557-023-01235-9.

Supplementary information The online version contains supplementary material available at https://doi.org/10.1038/s41557-023-01235-9.

Correspondence and requests for materials should be addressed to Wilhelm Boland or Michael Groll.

Peer review information *Nature Chemistry* thanks Kai Tittmann and the other, anonymous, reviewer(s) for their contribution to the peer review of this work.

https://doi.org/10.1038/s41557-023-01235-9

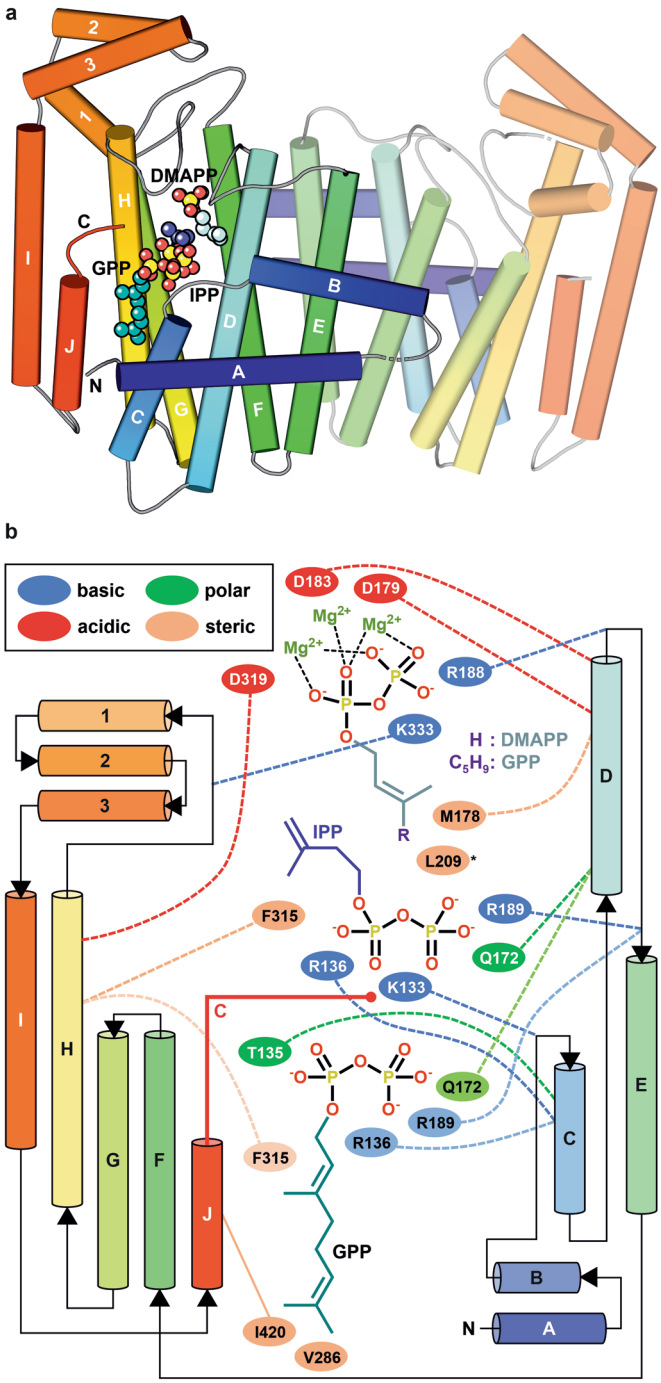

Extended Data Fig. 1 | Topology of *Pc*IDS1. a, Cartoon representation of *Pc*IDS1 with α-helices shown as cylinders in a spectrum from blue to red (N- to C-terminus). Helices are labelled from A-H, 1-3 and I-J. Sticks and balls representations of the natural ligands highlight their respective binding mode. **b**, Topology of the arrangement in a single subunit. The C_α chain trace is indicated by arrows. Residues coordinating ligands in the allylic (Al, cyan), homoallylic (HAl, purple) and allosteric (Allo, teal) site are connected to their respective position in the enzyme and coloured according to the nature of the interaction. An asterisk indicates a residue from the adjacent subunit. The C-terminus that orders upon binding of IPP_{HAl} or GPP_{Allo} is highlighted in red.

https://doi.org/10.1038/s41557-023-01235-9

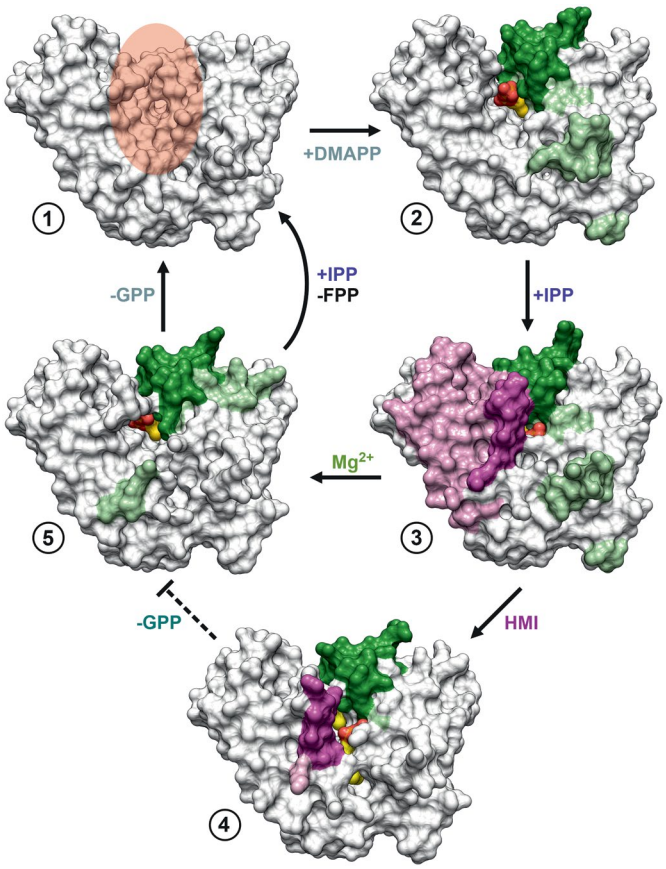

Extended Data Fig. 2 | Structural plasticity of *Pc*IDS1 during catalysis. Surface representations of *Pc*IDS1 subunits in complex with different ligands. The apo structure (**1**, PDB ID 8A6U) features a deep central cleft surrounded by disordered regions (highlighted in red). Upon binding of $DMAPP_{Al}$, the substrate loop between αD-E folds around the pyrophosphate (PP) moiety (**2**, PDB ID 8A6V, sub_A). Areas undergoing significant structural changes are shown in light green and residues disordered in the apo structure in dark green. The binding of IPP_{HAl} (**3**, PDB ID 8A6V, sub_B) shifts the peripheral domain around the SARM towards the active centre (light pink) and orders the region between αH-1 as well as the C-terminus (dark pink). The presence of heavy metal ions (HMI) stabilises the accommodation of an allosteric GPP molecule (**4**, PDB ID 8A73) that interferes with IPP_{HAl} binding. The C-terminus adapts a conformation as observed in the closed state. In absence of HMIs or upon release of GPP_{Allo}, the *Pc*IDS1:GPP complex (**5**, PDB ID 8A70) can either form FPP or start a new reaction cycle. Colour coding is described in *Materials and Methods*.

https://doi.org/10.1038/s41557-023-01235-9

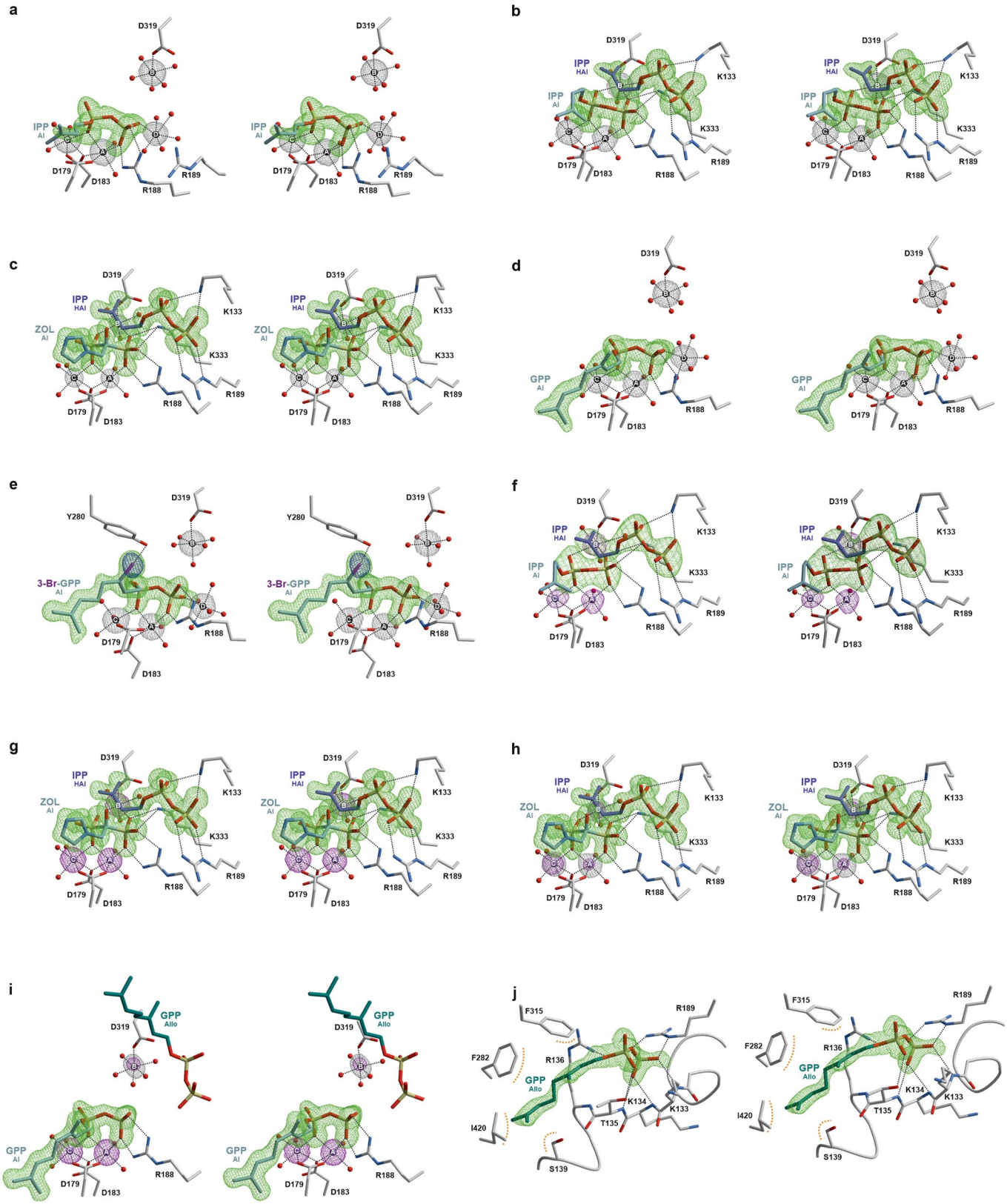

Extended Data Fig. 3 | Stereo views of *Pc*IDS1 structures. a-j. All representations according to Fig. 3.

https://doi.org/10.1038/s41557-023-01235-9

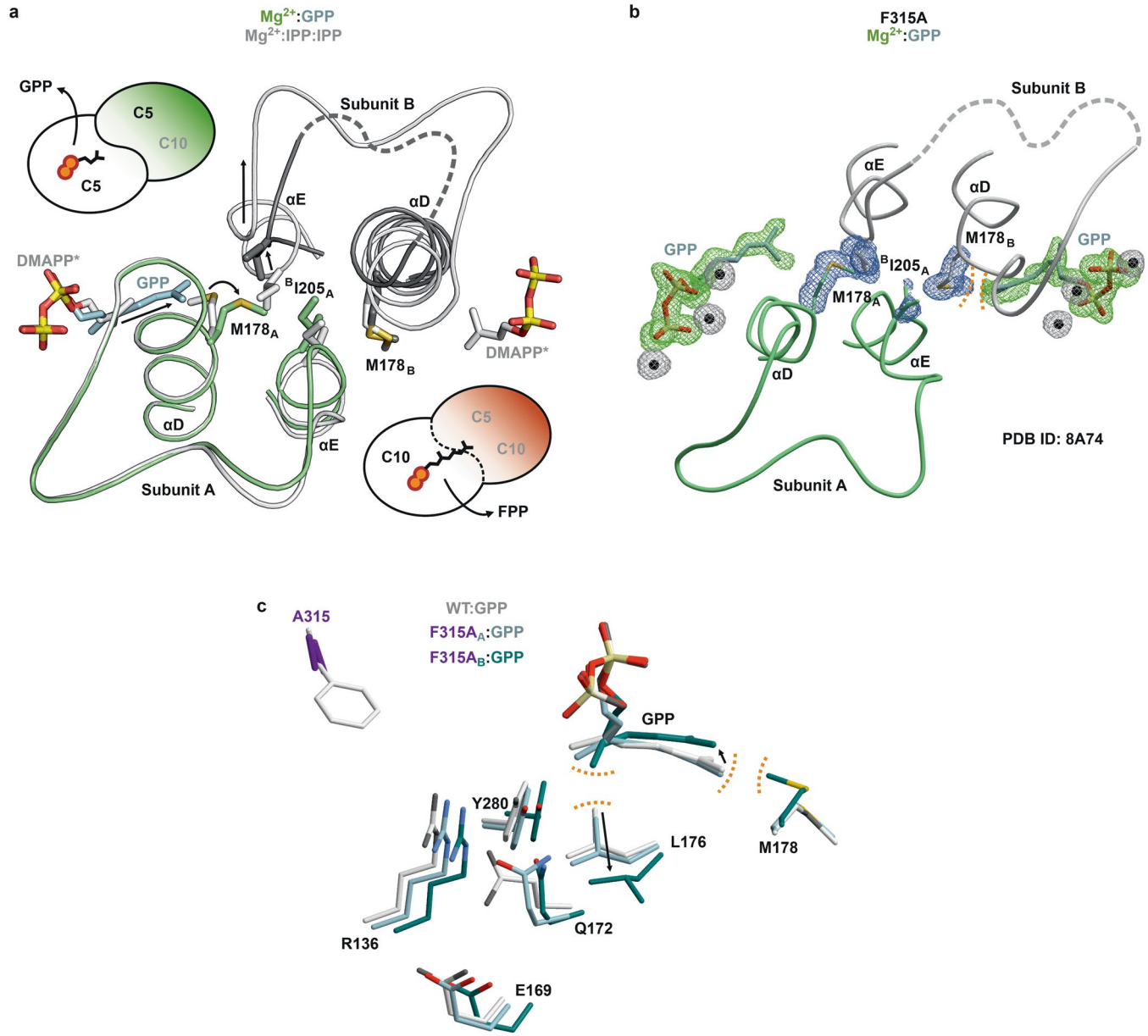

Extended Data Fig. 4 | GPP_{AI}-binding disrupts the substrate loop and HAI site in the neighbouring subunit. a, Superposition of *Pc*IDS1$_{Mg}$:GPP (coloured) and *Pc*IDS1$_{Mg}$:IPP:IPP (white, DMAPP* in the figure): The C_{10} prenyl chain of GPP_{AI} disrupts substrate loop formation in the neighbouring subunit by displacing $M178_A$ and $I205_B$, which disorders the N-terminus of αE_B. While GPP synthesis can take place synchronistically (top left scheme), the reaction to FPP can only occur successively (bottom right). **b**, *Pc*IDS1_F315A$_{Mg}$:GPP: In presence of GPP_{AI} in sub$_A$ (green), IPP_{HAI} coordination is prevented in sub$_B$ (grey). The FARM at the disrupted substrate loop retains affinity for allylic ligands. GPP_{AI} adopts a non-physiological, kinked conformation in sub$_B$ to avoid steric clashes (orange dashes) with M178. **c**, Superposition of *Pc*IDS1$_{Mg}$:GPP (grey) with sub$_A$ and sub$_B$ of *Pc*IDS1_F315A$_{Mg}$:GPP (cyan and teal): In absence of the phenyl sidechain, major rearrangements are observed for the regulatory network between R136, E169, Q172 and Y280. The kinked conformation of the GPP_{AI} moiety in F315A_B displaces L176 with its 3-methyl group (arrows). However, C_5 ligands would not interfere with M178 and L176 and could still bind to sub$_B$ in presence of GPP_{AI}. Colour coding is described in *Materials and Methods*.

nature portfolio

Corresponding author(s): Wilhelm Boland, Michael Groll

Last updated by author(s): May 8, 2023

Reporting Summary

Nature Portfolio wishes to improve the reproducibility of the work that we publish. This form provides structure for consistency and transparency in reporting. For further information on Nature Portfolio policies, see our Editorial Policies and the Editorial Policy Checklist.

Statistics

For all statistical analyses, confirm that the following items are present in the figure legend, table legend, main text, or Methods section.

n/a	Confirmed	
☐	☒	The exact sample size (*n*) for each experimental group/condition, given as a discrete number and unit of measurement
☐	☒	A statement on whether measurements were taken from distinct samples or whether the same sample was measured repeatedly
☒	☐	The statistical test(s) used AND whether they are one- or two-sided *Only common tests should be described solely by name; describe more complex techniques in the Methods section.*
☒	☐	A description of all covariates tested
☒	☐	A description of any assumptions or corrections, such as tests of normality and adjustment for multiple comparisons
☐	☒	A full description of the statistical parameters including central tendency (e.g. means) or other basic estimates (e.g. regression coefficient) AND variation (e.g. standard deviation) or associated estimates of uncertainty (e.g. confidence intervals)
☒	☐	For null hypothesis testing, the test statistic (e.g. *F*, *t*, *r*) with confidence intervals, effect sizes, degrees of freedom and *P* value noted *Give P values as exact values whenever suitable.*
☒	☐	For Bayesian analysis, information on the choice of priors and Markov chain Monte Carlo settings
☒	☐	For hierarchical and complex designs, identification of the appropriate level for tests and full reporting of outcomes
☒	☐	Estimates of effect sizes (e.g. Cohen's *d*, Pearson's *r*), indicating how they were calculated

Our web collection on statistics for biologists contains articles on many of the points above.

Software and code

Policy information about availability of computer code

Data collection	X06SA at the Swiss Light Source, Photon counting hybrid pixel area EIGER 16M (Dectris) detector, Albula 4.1
Data analysis	XDS/XSCALE (v. 2010), Phaser (v. 3.0), COOT (v. 0.8.7), REFMAC5 (v. 5.7), ARP/wARP (v. 7), CCP4 (Procheck, FFT; v 7.0), PyMol (v.2.3.5)

For manuscripts utilizing custom algorithms or software that are central to the research but not yet described in published literature, software must be made available to editors and reviewers. We strongly encourage code deposition in a community repository (e.g. GitHub). See the Nature Portfolio guidelines for submitting code & software for further information.

Data

Policy information about availability of data

All manuscripts must include a data availability statement. This statement should provide the following information, where applicable:

- Accession codes, unique identifiers, or web links for publicly available datasets
- A description of any restrictions on data availability
- For clinical datasets or third party data, please ensure that the statement adheres to our policy

Crystallographic data were deposited in the RCSB Protein Data Bank with the PDB IDs: 8A6U, 8A6V, 8A6Z, 8A70, 8A73, 8A74, 8A78, 8A7A, 8A7B, 8A7C, 8A7J, 8A7K, 8A7L, 8A7R, and 8A7U. All other data are available in the text or in the supplementary information.

Human research participants

Policy information about studies involving human research participants and Sex and Gender in Research.

Reporting on sex and gender	N/A
Population characteristics	N/A
Recruitment	N/A
Ethics oversight	N/A

Note that full information on the approval of the study protocol must also be provided in the manuscript.

Field-specific reporting

Please select the one below that is the best fit for your research. If you are not sure, read the appropriate sections before making your selection.

☒ Life sciences ☐ Behavioural & social sciences ☐ Ecological, evolutionary & environmental sciences

For a reference copy of the document with all sections, see nature.com/documents/nr-reporting-summary-flat.pdf

Life sciences study design

All studies must disclose on these points even when the disclosure is negative.

Sample size	No specific sample size was chosen, instead crystals were evaluated to diffract to 2.0 Å or better (if possible). All final x-ray data was measured from fifteen individual crystals. Thermal shift assays were performed screening all individual protein variants to the applied ligands at two different concentrations (replication see below).
Data exclusions	No data were excluded from biochemical or structural experiments.
Replication	Enzymatic assays were performed in triplicates and reliably reproduced. The final x-ray data sets were determined from fifteen individual crystals. Apart from the structural changes induced by different ligands, all obtained structures display a highly conserved and reproducible geometry.
Randomization	not applicable in our biochemical and crystallographic experiments
Blinding	not applicable in our biochemical and crystallographic experiments

Reporting for specific materials, systems and methods

We require information from authors about some types of materials, experimental systems and methods used in many studies. Here, indicate whether each material, system or method listed is relevant to your study. If you are not sure if a list item applies to your research, read the appropriate section before selecting a response.

Materials & experimental systems

n/a	Involved in the study
☒	☐ Antibodies
☒	☐ Eukaryotic cell lines
☒	☐ Palaeontology and archaeology
☒	☐ Animals and other organisms
☒	☐ Clinical data
☒	☐ Dual use research of concern

Methods

n/a	Involved in the study
☒	☐ ChIP-seq
☒	☐ Flow cytometry
☒	☐ MRI-based neuroimaging